PREDICTION OF COMPLEX FLOW PATTERNS IN INTRACRANIAL ATHEROSCLEROTIC DISEASE USING COMPUTATIONAL FLUID DYNAMICS

Clemens M. Schirmer, M.D.

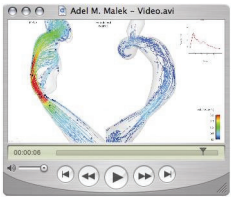
Department of Neurosurgery, Cerebrovascular and Endovascular Division, Tufts-New England Medical Center and Tufts University School of Medicine, Boston, Massachusetts

Adel M. Malek, M.D., Ph.D.

Department of Neurosurgery, Cerebrovascular and Endovascular Division, Tufts-New England Medical Center and Tufts University School of Medicine, Boston, Massachusetts

Reprint requests:
Adel M. Malek, M.D., Ph.D., Department of Neurosurgery, Tufts-New England Medical Center, 750 Washington Street, #178, Boston, MA 02111.
Email: amalek@tufts-nemc.org

Received, February 24, 2007.
Accepted, May 23, 2007.



ONLINE DIGITAL VIDEO

OBJECTIVE: Although carotid and vertebral intracranial atherosclerotic disease (ICAD) can lead to both hemodynamic insufficiency and thromboembolism, its fluid dynamic properties remain undefined because of its intricate features and complex three-dimensional geometry. We used computational fluid dynamic (CFD) analysis to model the hemodynamics of symptomatic ICAD lesions.

METHODS: Nine ICAD lesions (six carotid, two vertebral, one middle cerebral) underwent high-resolution catheter-based digital rotational angiography. The reconstructed three-dimensional volumes of the target lesions were segmented and used to generate hybrid computational meshes. Dynamic pulsatile CFD analysis was performed using a non-Newtonian shear-dependent model of blood's viscosity.

RESULTS: CFD results revealed complex flow patterns within ICAD lesions with mid-stenotic shear rates of greater than 19,000/s, sufficiently high to induce high-shear platelet activation. Vorticity and helicity within the stenoses were followed by sudden deceleration with formation of vortex cores. Pressure gradients were significant mostly at greater than 75% stenosis with a mean time-averaged drop of 27.2 ±17.8 mmHg. Unlike the smoothly-varying helicity imparted by the three-dimensional anatomy of the intracranial circulation, poststenotic regions of ICAD lesions showed significant and rapidly fluctuating helicity and vorticity patterns, which may contribute to the propagation of platelets activated by the high shear region within the stenosis throat. Stent angioplasty restored the hemodynamic profile of ICAD lesions to within contralateral controls.

CONCLUSION: Patient-based symptomatic ICAD lesions studied using CFD analysis appear to harbor a hemodynamically pathological environment that favors the activation, aggregation and distal embolization of platelets and is reversed by endovascular stent angioplasty.

KEY WORDS: Angioplasty, Computer simulation, Intracranial arteriosclerosis, Intracranial embolism and thrombosis

Neurosurgery 61:842–852, 2007 DOI: 10.1227/01.NEU.0000280081.68618.22 www.neurosurgery-online.com

Intracranial atherosclerosis (ICAD) of the carotid and vertebral artery of the cranial base and the intradural vessels of the circle of Willis is a progressive and dynamic disease (2). ICAD lesions can induce neurological symptoms by either hemodynamic insufficiency in vascular territories with poor collateral reserve or by thromboembolism through exuberant platelet activation or fragmentation of unstable plaque and mural thrombus (14, 15, 19, 26).

The complex irregular surface anatomy of stenotic lesions may lead to a disturbed flow pattern in time and space that possesses characteristics favoring abnormal activation of platelets within ICAD lesions and subsequent deposition and downstream embolization. Shear rate, the spatial gradient of the blood flow velocity field, or the velocity rate of change between infinitesimally thin layers of blood flow, is known to directly affect platelet function, with higher shear rates leading to activation (3, 4, 17). The interaction between shear rate and platelet activation involves a number of molecular pathways (17, 22), including sequential buildup of individual platelets on the surface of a thrombus followed by shape change, activation, and firm adhesion (28, 29, 32, 33). More recent results have demonstrated direct platelet aggregation by very high shear rates (>10,000/s), challenging the notion of sequential platelet accumulation and progressive activation followed by firm adhesion (30).

Computational fluid dynamic (CFD) analysis can provide insight into the spatial distribution of hemodynamic parameters

that are known to be transduced into altered platelet function and increased platelet activation (17, 22). Most CFD work has focused on idealized geometries with relatively low degrees of stenosis (8, 13, 37, 38), which may not be appropriate given the multiple sharp bends and bifurcations and complex spatial course of the intracranial arteries. In addition, the use of computed tomographic- and magnetic resonance-derived geometric models may not provide the requisite level of anatomic and luminal surface detail needed to accurately model the blood flow pattern. In an effort to better understand the microhemodynamic conditions and obtain an accurate temporal and spatial characterization of the flow within ICAD lesions, we have undertaken CFD analysis of actual patient-based vascular geometry obtained using high-resolution three-dimensional (3-D) rotational angiography.

PATIENTS AND METHODS

Patient Population

Nine patients (*Table 1*) presented for angiographic evaluation with ICAD of the internal carotid artery in six patients, of the vertebral artery in two patients, and of the middle cerebral artery in one patient (*Fig. 1A*). The patients underwent catheter-based digital subtraction cerebral angiography in biplane and 3-D rotational modes (12). The mean angiographic stenosis ranged between 53 and 95% (mean, 75%) by the Warfarin-Aspirin Symptomatic Intracranial Disease (WASID) criteria (31). Seven patients (Patients 1, 2, and 4–8) underwent subsequent percutaneous transluminal angioplasty and stenting (PTAS) followed by identical image acquisition.

Mesh Generation

3-D volumetric datasets obtained from the backprojection reconstruction of the rotational angiograms were available for all nine patients before treatment and for five of the seven treated patients after PTAS (Patients 1, 2, 4, 6, and 8). The contralateral internal carotid artery was available as a 3-D dataset in four patients (*Table 1*). These datasets were segmented and used as input for the generation of a hybrid, predominantly hexahedral, mesh. Because of the sensitivity of segmentation to the thresholding and windowing of the data, the resulting mesh (*Fig. 1B*) was verified in its dimensions against the concurrently acquired conventional biplane angiographic projections to ensure true representation of the vessel geometry. A typical mesh contained approximately 400,000 cells with an entrance length measuring at least 10 ves-

TABLE 1. Demographic features, presenting symptoms, location, and computed pressure drop of the lesion of patients harboring symptomatic intracranial atherosclerotic disease lesions in this series[a]

Patient no.	Age (yr)/ sex	Stenosis location	Clinical presentation	Stent type[b] dimension	Angiographic stenosis (%)	Contralateral vessel available	Δp Peak systole (mmHg)	Δp End diastole (mmHg)
1	49/F	Left petrous ICA	TIA, left hemisphericcontralateral ICA occlusion	Cordis Bx Sonic 3.5 × 18 mm	70	—	23	5
2	56/M	Left petrous ICA	TIA of right arm and face, in preparation for cardiac surgery found to have left ICA stenosis	Cordis Bx Velocity 3.5 × 13 mm	70	Yes	147	22
3	56/F	Right cavernous ICA	TIA right eye and left arm with previous MRI infarcts in right hemisphere	—	70	Yes	30	7
4	69/M	Right petrous ICA	TIA during episode of transient hypotension	Medtronic AVE S7 3.5 × 9 mm	>90	—	94	18
5	76/M	Left petrous ICA	TIA, left arm weakness	Medtronic Driver 4 × 12 mm[c]	80	Yes	83	15
6	55/M	Right petrous ICA	Decreased right ocular acuity	Medtronic Driver 4 × 12 mm	>90	Yes	288	44
7	75/M	Right VA	Progressive lightheadedness and dizziness	Boston Scientific Wingspan 3.5 × 15 mm[c]	90	—	124	14
8	67/M	Left VA	SAH Grade V, fusiform aneurysm and severe intracranial atherosclerosis of left VA	Medtronic AVE S7 2.5 × 15 mm and 2.5 × 9 mm	70	—	94	10
9	64/F	Left MCA M1 segment	TIA, left hemispheric	—	55	—	21	5

[a] ICA, internal carotid artery; TIA, transient ischemic attack; MRI, magnetic resonance imaging; VA, vertebral artery; SAH, subarachnoid hemorrhage; MCA, middle cerebral artery.
[b] Stent types included the following: Wingspan Stent (Boston Scientific, Natick, MA); Bx Sonic and Bx Velocity Stent (Cordis Endovascular, Miami Lakes, FL); AVE S7 and Driver OTW Stent (Medtronic, Minneapolis, MN).
[c] No posttreatment rotational angiogram available.

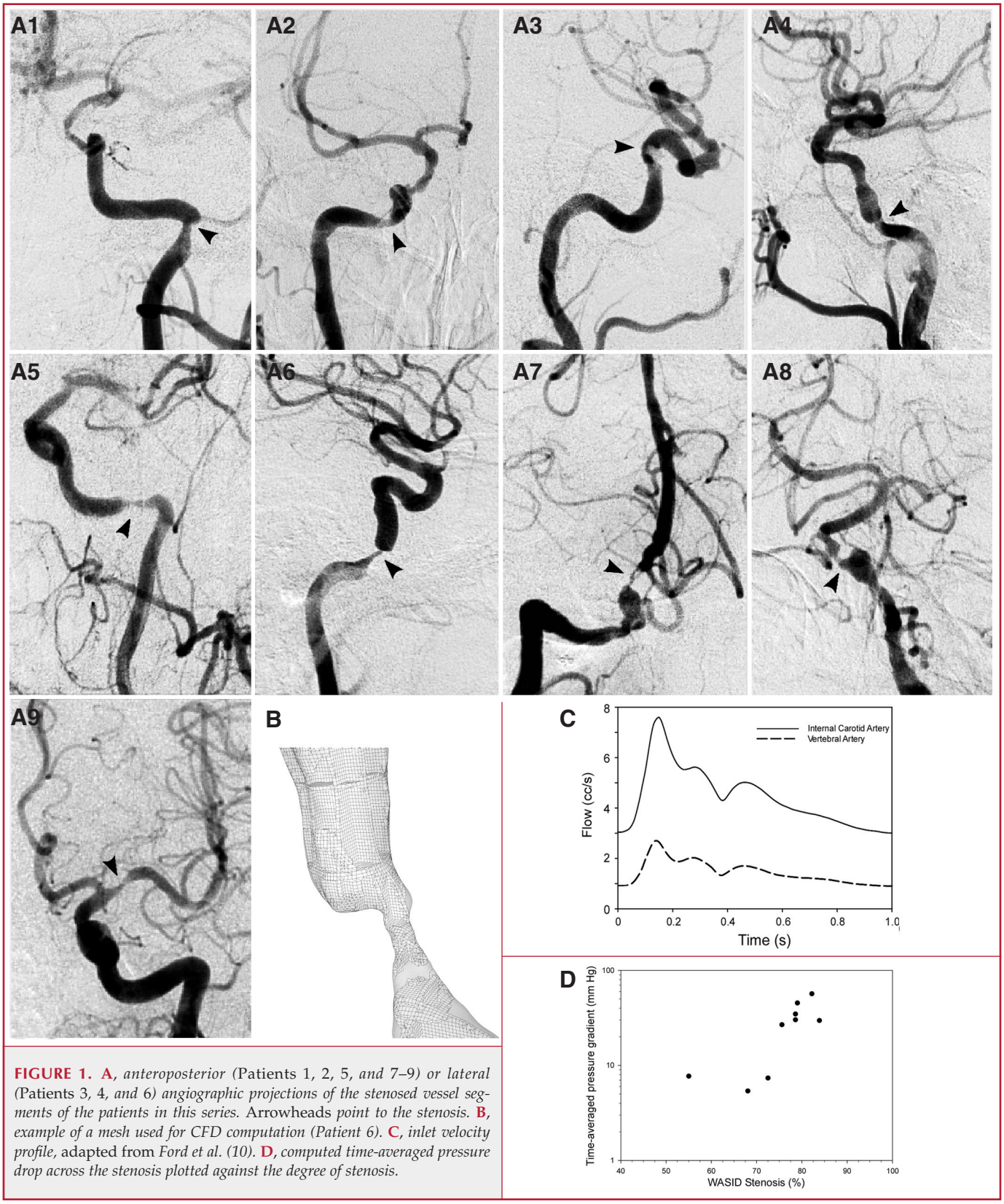


FIGURE 1. **A**, *anteroposterior* (Patients 1, 2, 5, *and* 7–9) *or lateral* (Patients 3, 4, *and* 6) *angiographic projections of the stenosed vessel segments of the patients in this series.* Arrowheads *point to the stenosis.* **B**, *example of a mesh used for CFD computation (Patient 6).* **C**, *inlet velocity profile,* adapted from *Ford et al. (10).* **D**, *computed time-averaged pressure drop across the stenosis plotted against the degree of stenosis.*

sel diameters upstream of the stenosis to ensure development of a Womersley flow profile (41) in the prestenotic segment. Models of an idealized stenosis of 25, 50, and 75% were generated as a straight tube of 120 mm length and 4 mm diameter with a smooth stenosis located 50 mm downstream from the inflow (36).

Non-Newtonian Blood Rheology

In arterial vessels, the non-Newtonian features of blood can be represented mainly by its shear-thinning properties; its viscoelasticity may be ignored (11). The shear-thinning viscosity of blood was captured using the Carreau-Yasuda model (5) with parameters derived from a best fit to experimental data obtained on analog blood fluid (11). The Carreau model accurately describes the properties of blood (11, 27) and may be written as

$$\mu(\dot{\gamma}) = \mu_\infty + (\mu_0 - \mu_\infty)\left[1 + (\lambda\dot{\gamma})^2\right]^{(n-1)/2}$$

where μ_∞ and μ_0 designate the viscosity at infinite and zero shear rates, respectively, λ is the time constant of the shear-dependent viscosity change, n is the index of the power law, and γ is the shear rate. The following parameter values were used to ensure best fit with previous experimental data (11, 40): $\mu_\infty = 0.0037$ Pas, $\mu_0 = 0.0314$ Pas, $\lambda = 2.517$ seconds, and $n = 0.5736$.

Computational Fluid Dynamic Analysis

CFD analysis was carried out using Fluent software (version 6.2.16; Fluent Inc., Lebanon, NH) on a cluster of parallel computers in the Windows environment (versions XP64 and XP; Microsoft Corp., Redmond, WA) using the double-precision 3-D solver in laminar unsteady regime. The vessel wall was assumed to be rigid, and velocity conditions obeyed nonslip and nonpenetration constraints at the wall. A 500-timestep pulsatile flow waveform (*Fig. 1C*) was derived from the waveforms previously described in healthy human subjects by Ford et al. (10) and prescribed at the inlet for unsteady simulations. For internal carotid lesions, the time-average inlet velocity was 0.25 m/sec based on an inlet cross sectional area of 18.1 mm^2 and volume flow rate of 4.58 ml/sec, with a Reynolds number of 371 and a Womersley (41) number of 3.3. For vertebral artery lesions, the time-average inlet velocity was 0.17 m/sec based on an inlet cross-sectional area of 9.08 mm^2 (35) and a volume flow rate of 1.52 cc/sec (10), with a Reynolds number of 173 and a Womersley number of 2.4.

Validation of Computational Approach

We previously validated our computational approach using experimental data by Ahmed and Giddens (1) using pulsatile flow through a straight tube with an axisymmetric smooth cosine-shaped stenosis of 75% cross-sectional area reduction with excellent agreement (36). We also evaluated the dependence of our results on grid density using the model of ICAD lesions. Meshes with 35×10^3 to 840×10^3 elements were created for a fixed geometry and the simulation results using these compared. No significant difference was observed beyond a mesh of 201×10^3 elements in velocity and shear stress distributions. We chose a target mesh size of 400×10^3 elements to optimize the accuracy of gradient derivatives and computational time. The velocity magnitude and wall shear stress were also compared at two cross-sectional profiles upstream and downstream of the stenosis after two and three cycles of waveform computation; only small changes were seen when comparing results after the second and third cycle iterations (2.2% for centerline velocities and 2.4% for wall shear stress). Accordingly, the results were analyzed after the three iterations of the pulsatile waveform.

Postprocessing and Statistics

Postprocessing was performed using Ensight software (version 8; Computational Engineering International, Apex, NC). Cut planes were chosen perpendicular to the axial direction of flow in the throat of the stenosis, as well as the pre- and post-stenotic regions, and were used for analysis of shear rate, vorticity, and helicity. Statistical analysis was performed using SAS software (SAS software, Cary, NC), with significance assumed for a P value of less than 0.05.

RESULTS

Pressure Gradient Across ICAD Lesions

The time-averaged pressure gradient across the ICAD lesions was measured in the computational model at points three vessel diameters proximal and distal to the stenosis over an entire cardiac cycle. The pressure gradient was found to increase significantly for stenoses greater than 75% (*Fig. 1D*). The time-averaged mean pressure drop across all patients was 27.2 $\pm$ 17.8 mmHg. The instantaneous mean pressure drop was 100 $\pm$ 83 mmHg during peak systole (pS) and 16 $\pm$ 12 mmHg during end diastole (eD) (*Table 1*).

Flow Velocity Pattern

(see videos at web site)

Pathlines and two-dimensional cut planes through the throat of the stenosis are shown for four lesions (*Fig. 2A*; *Video 1*) and two controls (*Fig. 2B*), colored by the systolic velocity. Flow changes common to all lesions studied here can be grouped into five distinct events. The first involves the region of the throat of the stenosis at which the flow is accelerated and forms a jet that is further pronounced during systole. Secondly, we observe the onset of flow separation into a retrograde component which begins in the distal end of the stenosis and spreads centrifugally from the central jet (*black arrowheads*). The third represents the zone of flow recirculation, which is characterized by low flow. The residence time of virtual particles is increased in this recirculation zone of stasis (*Video 2*). In cases in which the stenosis is located proximal to a sharp bend in the vessel, the high-velocity flow jet remains adherent to the vessel wall on one side with an accentuation of the recirculation on the opposite wall (Patients 2 and 6) (*Video 1*) when compared with symmetric recirculation surrounding the central jet in stenoses within straight segments (Patients 4 and 7). Within the zones of recirculation, the fourth event involves the formation of vortices, which exhibit dynamic changes in size and location during the cardiac cycle (Patient 7) (*Fig. 2A*). In the fifth section, the retrograde flow reattaches with reconstitution of laminar flow distally (*stars*). In contrast, evaluation of the flow pattern in the contralateral controls reveals a near-laminar flow pattern with small irregularities (*Fig. 2B*, *star*), as a consequence of the normal 3-D curvature of the intracranial vessels, which is maintained over the course of the cardiac cycle (*Fig. 2B; Video* 1).

Intraluminal Shear Rate

The shear rate was highest at the level of the stenosis throat (*Fig. 3A, black arrowheads*; *Video 3*). In cases of asymmetric steno-

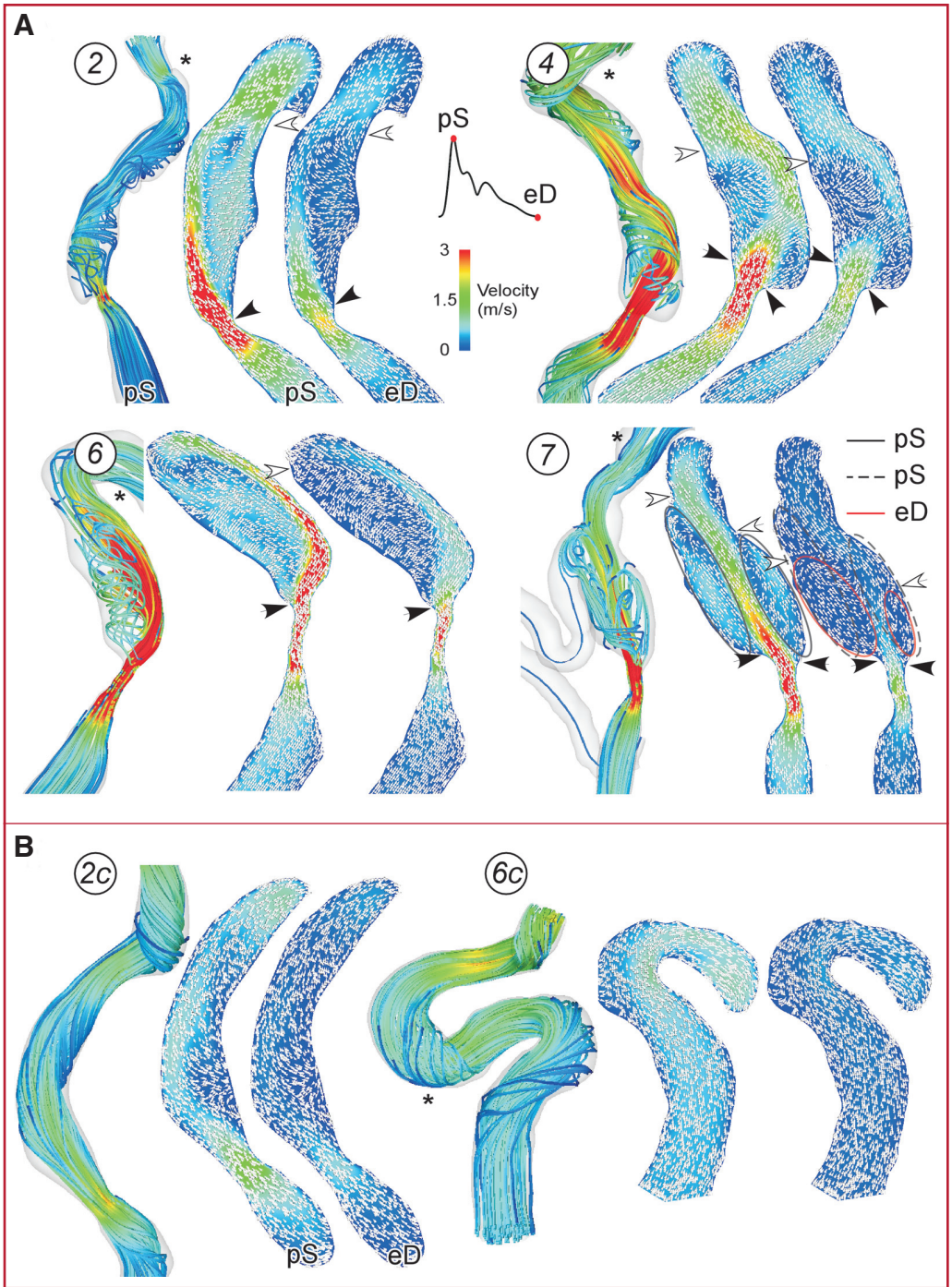


FIGURE 2. A, *examples for pathlines and unscaled unity velocity vectors on a longitudinal cut plane during peak systole* (pS) *and end diastole* (eD), *color-coded for velocity magnitude* (Patients 2, 4, 6, *and 7).* Black arrowheads *indicate points of flow separation,* white arrowheads *indicate reattachment of the flow, and* stars *indicate return to laminar flow. On the cut planes for Patient 7, the recirculation vortices are marked during pS* (black ellipses) *and eD* (red ellipses). Dashed ellipses *indicate the position of the* black ellipses *(pS) for comparison.* **B**, *pathlines and unscaled unity velocity vectors on a longitudinal cutplane in the contralateral control internal carotid artery of Patients 2 and 6 for comparison. The* star *indicates one instance of twisting of the pathlines as a consequence of the 3-D intracranial vascular geometry.*

sis or in central symmetric ICAD lesions just proximal to a vessel bend, the elevated shear rate extended to the lateral wall (*Fig. 3A, white arrowheads*). Histogram analysis of axial cross-sections revealed that peak shear rates were approximately 10 times greater in ICAD lesions before PTAS at the throat of the ICAD stenoses (*Fig. 3B*); among all ICAD stenosis throats, average shear rate showed significant variation between 19,070 ± 15,777 seconds^{-1} at pS and 7674 ± 6538 seconds^{-1} at eD before treatment. PTAS decreased the average shear rate significantly to 886 ± 906 seconds^{-1} (pS) and 318 ± 288 seconds^{-1} (eD) ($P < 0.0001$). The distribution of shear rate before PTAS is broader and better defined after treatment, as evidenced by the smoother drop-off of values in the double-logarithmic plot in *Figure 3B*). Before PTAS, the shear rates in the poststenotic recirculation were, as expected, significantly lower than within the throat of the stenosis ($P < 0.0001$) (*Table 2*). Shear rates in the contralateral vessels were slightly higher than those within the target ICAD lesion after PTAS. It should be noted that the contralateral vessels were affected by mild to moderate atherosclerotic changes, which led to small irregularities of the flow and increased shear rates (Patients 2C and 5C) (*Fig. 3A*).

Given the documented higher rate of clinical events from patients with ICAD stenosis of greater than 70% compared with less than 70% (14), we sought to evaluate the effect of stenosis rate on shear rate. Accordingly, shear rates in a model of an idealized 25, 50, and 75% stenosis were computed to allow uncoupling of the effect of the patient-specific

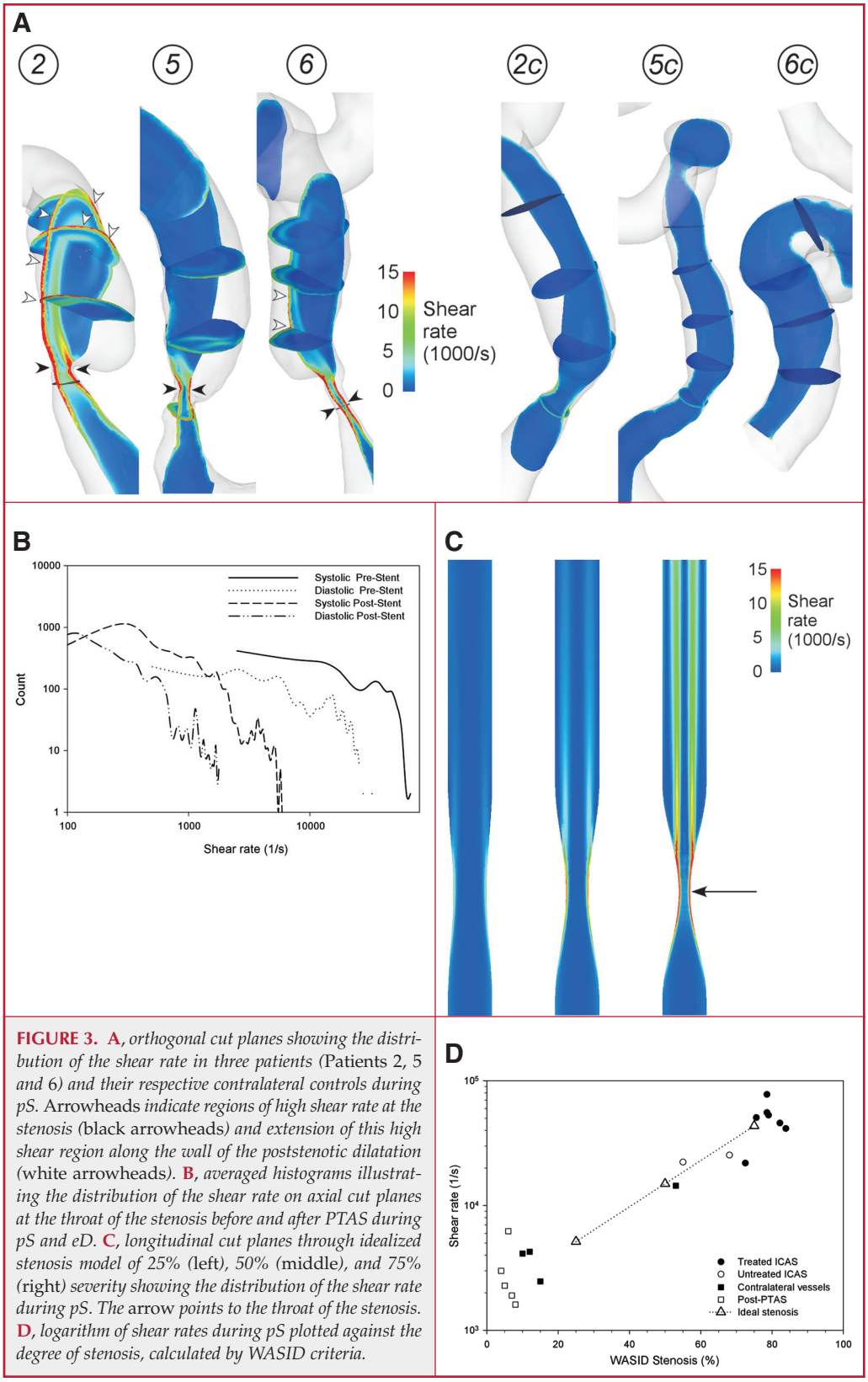


FIGURE 3. **A**, *orthogonal cut planes showing the distribution of the shear rate in three patients* (Patients 2, 5 *and* 6) *and their respective contralateral controls during pS.* Arrowheads *indicate regions of high shear rate at the stenosis* (black arrowheads) *and extension of this high shear region along the wall of the poststenotic dilatation* (white arrowheads). **B**, *averaged histograms illustrating the distribution of the shear rate on axial cut planes at the throat of the stenosis before and after PTAS during pS and eD.* **C**, *longitudinal cut planes through idealized stenosis model of 25%* (left), *50%* (middle), *and 75%* (right) *severity showing the distribution of the shear rate during pS. The* arrow *points to the throat of the stenosis.* **D**, *logarithm of shear rates during pS plotted against the degree of stenosis, calculated by WASID criteria.*

lesion geometry from the effect of the stenosis. In the model of a 25% stenosis, the average shear rates at the throat of the stenosis were 5144/second (pS) and 867/second (eD), increasing to 14,967/second (pS) and 3287/second (eD) for 50% stenosis, and 43,500/second (pS) and 25,163/second (eD) for 75% stenosis (*Fig. 3C*).

Peak shear rates in the target stenosis, the contralateral control vessel, the target stenosis following PTAS, and the idealized stenosis were plotted in a logarithmic fashion against the degree of stenosis. Logarithms of the peak shear rates ranged from 21,914/second to 77,813/second in the stenosis (*Fig. 3D*) during pS and from 6613/second to 33,104/second (not shown) during eD; these values were found to be proportional to the degree of stenosis (proportionality factors are 0.040 and 0.044 for shear rates during pS and eD, respectively; $P < 0.0001$ for both). The seven lesions that underwent PTAS displayed higher shear values compared with the two lesions that were not treated (*Fig. 3D*).

Flow Vorticity in ICAD Lesions

Vorticity is a measure of the rotatory component of blood flow, which can facilitate the visualization of vortex cores. Vortex shedding in a region of high vorticity in the region of flow separation has been implicated in the pattern of platelet deposition in vitro (6, 7). Orthogonal cut planes through the lumen of three illustrative cases and contralateral controls is shown in *Figure 4A* (*Video 4*). Regions of high vorticity delimit the jet of accelerated flow at the throat of the stenosis and in the poststenotic region. Complex progression of these regions of increased vorticity

TABLE 2. Shear rate and vorticity comparison[a]

Sampling location	Phase of cardiac cycle	Shear rate (1/s)	*P* value (versus stenotic value)	Vorticity (m/s)	*P* value (versus stenotic value)
Stenosis (n = 9)	pS	19070 ± 15777		17829 ± 15515	
	eD	7674 ± 6538	0.000005	7339 ± 6509	0.000005
Poststenotic dilatation (n = 9)	pS	2997 ± 3921	0.000005	2912 ± 3615	0.000005
	eD	839 ± 1012	0.000005	828 ± 950	0.000005
Contralateral control (n = 4)	pS	1533 ± 2181	0.000005	1023 ± 953	0.000005
	eD	532 ± 732	0.000005	348 ± 263	0.000005
Post PTAS (n = 5)	pS	886 ± 906	0.000005	879 ± 902	0.000005
	eD	318 ± 288	0.000005	319 ± 291	0.000005

[a] pS, peak systole; eD, end diastole; PTAS, percutaneous transluminal angioplasty and stenting.

along the curvature of the poststenotic region can be seen in the stenotic cases (*white arrowheads*). In contrast, regions of only mildly increased vorticity line the wall of the contralateral control vessels (*Fig. 4A*; *Video 4*). The temporal evolution of the vorticity magnitude in the lumen of the ICAD lesions vessel is not easily depicted by static snapshots; the differences between peak-systole and end-diastole are significant (*Video 4*). Sampling the distribution of vorticity vectors at the throat of the stenosis yielded an average vorticity magnitude 17,829 ± 15,515 seconds^{-1} during pS and 7339 ± 6509 seconds^{-1} during eD ($P < 0.0001$) (*Table 2*). PTAS decreased the vorticity magnitude significantly to 879 ± 902 seconds^{-1} during pS and 319 ± 291 seconds^{-1} during eD ($P < 0.0001$) (*Fig. 4B*). PTAS restored the vorticity magnitude at the throat of the stenosis to a level comparable to vorticity values in the contralateral control vessels 1023 ± 953 seconds^{-1} during pS and 348 ± 263 seconds^{-1} during eD (*Fig. 4C*; *Table 2*).

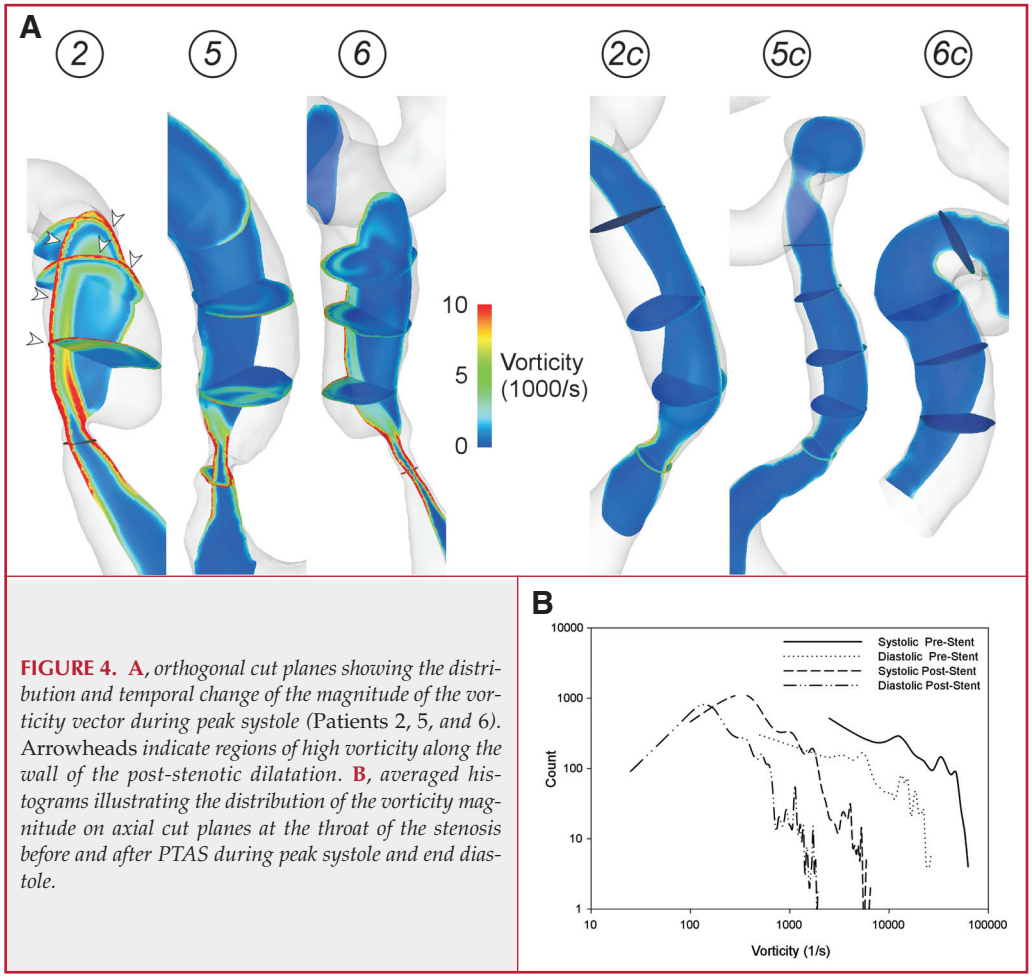


FIGURE 4. A, *orthogonal cut planes showing the distribution and temporal change of the magnitude of the vorticity vector during peak systole* (Patients 2, 5, *and* 6). Arrowheads *indicate regions of high vorticity along the wall of the post-stenotic dilatation.* **B**, *averaged histograms illustrating the distribution of the vorticity magnitude on axial cut planes at the throat of the stenosis before and after PTAS during peak systole and end diastole.*

Flow Helicity Along Pathlines

Complex 3-D flows, particularly twisting and curling of the pathlines of the flow, can be characterized using the helicity density as a pseudo scalar quantity (23). Evaluation of the control vessels (*Fig. 5A*) demonstrates the presence of smoothly varying helicity along the pathlines as the blood flow negotiates the complex curves and bends of the intracranial anatomy. In contrast, evaluation of the helicity along the pathlines in ICAD lesions (*Fig. 5A*) demonstrates very focal and rapid changes in helicity induced by the lesion (*Video 5*). These

increases in helicity, characterized by a split in the pathlines into a right- and left-handed corkscrew component begin over a very short distance and extend well distally to the throat into the poststenotic region (Patients 2 and 6) (*Fig. 5A*). Further downstream, the two corkscrew components merge again and continue the laminar smoothly-varying helicity pattern observed in the anatomy of contralateral control vessels.

Evaluation of the helicity distributions were computed (*Fig. 5B*), showing a wide variation during the cardiac cycle with one order of magnitude difference between -179 ± 4303 m^2/s^2 at pS and -9 ± 432 m^2/s^2 at eD (not significant, $P = 0.057$). PTAS significantly decreased the peak helicity density and shifted the histogram toward a lower helicity of 10 ± 141 m^2/s^2 during pS and 1 ± 21 m^2/s^2 during eD ($P < 0.005$) (*Fig. 5B*). The helicity distribution in the contralateral control side was 81 ± 246 m^2/s^2, significantly higher than the shear distribution after stenting ($P < 0.0001$), with both approximately one order of magnitude lower than before PTAS (*Fig. 5C*).

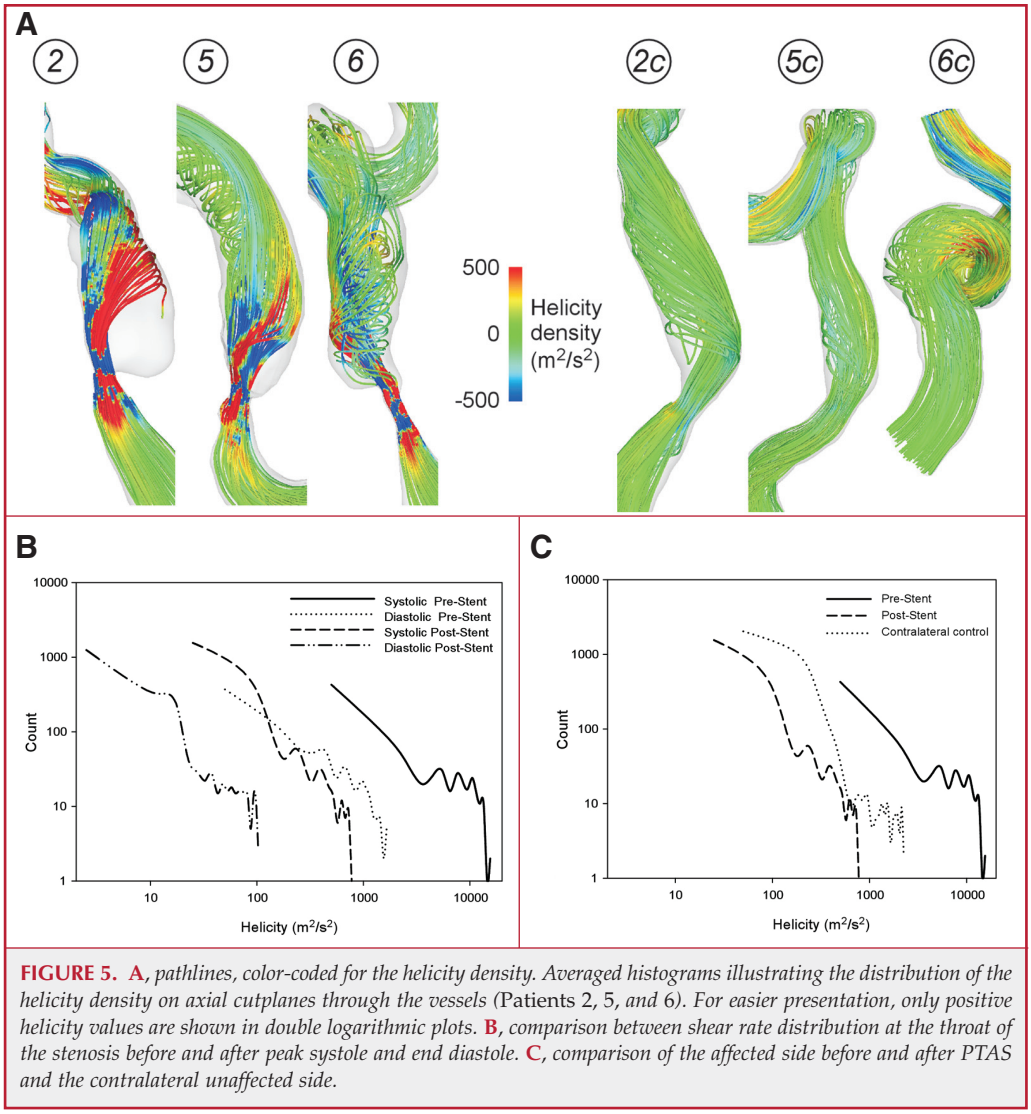


FIGURE 5. A, *pathlines, color-coded for the helicity density. Averaged histograms illustrating the distribution of the helicity density on axial cutplanes through the vessels* (Patients 2, 5, *and 6). For easier presentation, only positive helicity values are shown in double logarithmic plots.* **B**, *comparison between shear rate distribution at the throat of the stenosis before and after peak systole and end diastole.* **C**, *comparison of the affected side before and after PTAS and the contralateral unaffected side.*

DISCUSSION

The current study aimed to bridge the gap between benchtop hemodynamic simulations and experiments of smooth idealized stenosis and actual patient-based intracranial atherosclerosis lesions, with the objective of better understanding the prevailing local hemodynamics contributing to pathological thromboembolism and stenosis progression. Both endothelial cells and platelets are known to be exquisitely regulated by local shear stress and shear rate, respectively. Our results demonstrated, for the first time, the patterns of intraluminal shear rate, vorticity, and helicity within the intracranial circulation in control and ICAD-affected vessel segments. We found that even control vessels exhibited significant helicity, mild vorticity, and some flow separation as a result of the tortuous intracranial anatomy. These mild changes were dwarfed by the pathologically high shear rate with the throat of ICAD lesions and the ensuing dynamically complex vorticity and helicity; we also employed the same technique to evaluate post-PTAS hemodynamics and confirm resolution of the pathological hemodynamic features by endovascular treatment.

Severe ICAD is associated with a significant risk of persistent neurological symptoms and stroke, despite maximal medical therapy (14, 15, 26). These neurological events can result from either thromboembolic events or from hemodynamic insufficiency. Medical therapy with antiplatelet and anticoagulant therapy is only partially effective against thromboembolic phenomena and is largely futile in cases of insufficiency. We were able to compute the pressure drop across the stenosis in our models. Although there was a clear increase of the pressure drop with increasing stenosis, there was no simple correlation with formulas that predict the pressure drop in larger arteries (42), a finding which is corroborated by data from coronary arteries that are approximately the same diameter as the

intracranial internal carotid and vertebral arteries (16). Evaluation of the pressure gradient across ICAD lesions derived from CFD analysis rather than approximation may aid in the decision-making process to offer surgical bypass grafting from the extracranial to intracranial circulation (24, 25) or PTAS in lesions suspected of causing hemodynamic insufficiency. Examination of intracranial stenotic vessels with CFD analysis allows a more direct and potentially more accurate estimation of flow descriptors such as the velocity of the fluid jet in the stenosis and the pressure drop across the stenosis. The location of ICAD lesions in the cranial base and cranial vault makes noninvasive detection of these values difficult, whereas invasive methods such as microcatheter-based pressure measurement or microwire-based intravascular ultrasound remain invasive and potentially risky. The characterization of ICAD lesions using CFD analysis, in addition to degree of stenosis or to simplistic qualitative lesion features, may offer a more accurate and useful assessment of its embologenic potential or its risk of progression; a prospective analysis of patients with ICAD lesions undergoing 3-D imaging may help evaluate the usefulness of CFD analysis in risk stratification. We found a simple exponential relationship between the shear rate in the throat of the stenotic vessels examined and the degree of stenosis at the point of measure (*Fig. 3D*), which also compared well with the shear rates found in models of an idealized stenosis. A recent analysis of the data gathered during the WASID study showed an approximate twofold increased risk for a stroke in patients with stenosis greater than 70% (14). Our data suggest that greater than 70% stenosis predicts shear rates greater than 10,000/second, a range of shear rate known to increase the propensity for platelet activation.

The approach taken in the current study focused on modeling the hemodynamic conditions within the flow channel that blood and its elements would encounter rather than on the shear stress generated by the flow on the vessel wall. We are currently investigating the latter, which is more likely to play a role in lesion progression or rupture. Like all modeling approaches, this reductionist approach does not account for the complex multicellular autocrine and paracrine interactions among the various vessel wall cells and components.

Our current modeling technique has other limitations, including the assumption of a rigid wall (20) and ignores plaque composition and heterogeneity; it is accordingly less well suited at evaluating the stresses within vulnerable plaque such as recently demonstrated by Li et al. (19). Analysis of the viscoelastic and probably nonuniform spatial properties of an atherosclerotic vessel wall would necessitate a knowledge of not only lesion geometry but also a definition of the components of its heterogeneous material composition and their material properties. Such an analysis would require the use of fluid-structure interaction techniques, which offer a solution by taking the deformation of the computational mesh by the prevailing pressure field iteratively into account, resulting in a considerably larger computational requirement. Previous fluid-structure interaction analysis of a vessel stenosis utilized a smaller grid size of 32,000 cells (39) (compared with ~400,000 cells in this study), which would be insufficient to study the details of the flow in the poststenotic region. It is unclear whether or not the assumption of an elastic wall would fundamentally alter the basic premise of our findings; a recent study of wall stress in a model of an abdominal aortic aneurysm showed minimal difference (on the order of 1%) between the rigid and elastic-wall (fluid-structure interaction) models (18). Nonetheless, our results predicted for the first time in actual patient-based lesions the presence of very high shear rates (>10,000/s) recently shown to induce platelet adhesion and aggregation, even in the absence of platelet activation (30). Previous work has shown that shear rate can directly activate platelets (3, 4, 17) via a number of molecular pathways (17, 22), leading to a sequential buildup of individual platelets on the surface of a thrombus followed by shape change, activation, and firm adhesion (28, 29, 32, 33). The role of shear rate as a modulating factor of platelet function is well established over a wide range of flow conditions that includes pathological states leading to thrombus formation (22). Platelet aggregation at physiological shear rates (1000–10,000/s) involves the temporal succession of two phases, shear-induced formation of membrane tethers followed by platelet shape change and irreversible adhesion. The reactivity of the thrombogenic surface, the level of shear stress, and the density of the platelets at the adhesive surface were found to be determinants of the conversion of a reversible discoid platelet aggregates to stable aggregation (22). This model does not account for the development of stable aggregates in higher shear conditions (>10,000/s), commonly encountered in the jet in the stenosis in this series. A mechanism mediating aggregation of the smooth spherical platelets, a morphology assumed under high shear (21, 30), has been described recently (22), supporting that even under the highly pathological shear conditions encountered in high-degree stenosis, activation and stable aggregation occurs, which can persist for minutes (30). This may explain the finding in an analysis of the WASID data that showed significantly increased ischemic stroke rates in the vascular bed of a stenotic vessel with greater than 70% stenosis. High shear conditions that are encountered in stenotic vessels may not invariably result in acute thrombosis of the vessel because of the shear stress modulation of endothelial function, including release of nitric oxide and prostacyclin that counteract platelet aggregation (9, 34). Endothelial dysfunction from metabolic syndrome (26) and atherosclerotic plaques in the zone of high shear may prevent this physiological response. Caution should be exercised not to generalize the findings from the current study to different patient populations because of the inherent heterogeneous features of intracranial stenosis. The current study focused on the possible effects of hemodynamic condition within ICAD stenosis on platelet activation and embolization; this mechanism is only one component of possible sources which includes ruptured plaque fragments and cholesterol debris.

CONCLUSION

In conclusion, this study uncovered the pathological hemodynamic conditions prevailing in ICAD lesions using CFD

analysis and has modeled predicted shear rates that are sufficiently elevated to induce direct platelet aggregation and a poststenotic environment that favors further propagation. These results suggest future studies to evaluate the use of the current CFD approach for risk stratification and as a predictor of ICAD progression or recurrence after endovascular treatment in a patient-based lesion-specific manner.

REFERENCES

1. Ahmed SA, Giddens DP: Pulsatile poststenotic flow studies with laser Doppler anemometry. **J Biomech** 17:695–705, 1984.
2. Akins PT, Pilgram TK, Cross DT 3rd, Moran CJ: Natural history of stenosis from intracranial atherosclerosis by serial angiography. **Stroke** 29:433–438, 1998.
3. Anderson GH, Hellums JD, Moake J, Alfrey CP Jr: Platelet response to shear stress: Changes in serotonin uptake, serotonin release, and ADP induced aggregation. **Thromb Res** 13:1039–1047, 1978.
4. Anderson GH, Hellums JD, Moake JL, Alfrey CP Jr: Platelet lysis and aggregation in shear fields. **Blood Cells** 4:499–511, 1978.
5. Bird RB, Armstrong RC, Hassager O: *Dynamics of Polymer Liquids*. New York, Wiley, 1987, pp 169–175.
6. Bluestein D, Gutierrez C, Londono M, Schoephoerster RT: Vortex shedding in steady flow through a model of an arterial stenosis and its relevance to mural platelet deposition. **Ann Biomed Eng** 27:763–773, 1999.
7. Bluestein D, Niu L, Schoephoerster RT, Dewanjee MK: Fluid mechanics of arterial stenosis: Relationship to the development of mural thrombus. **Ann Biomed Eng** 25:344–356, 1997.
8. Buchanan JR, Kleinstreuer C, Comer JK: Rheological effects on pulsatile hemodynamics in a stenosed tube. **Computers & Fluids** 29:695–724, 2000.
9. de Graaf JC, Banga JD, Moncada S, Palmer RM, de Groot PG, Sixma JJ: Nitric oxide functions as an inhibitor of platelet adhesion under flow conditions. **Circulation** 85:2284–2290, 1992.
10. Ford MD, Alperin N, Lee SH, Holdsworth DW, Steinman DA: Characterization of volumetric flow rate waveforms in the normal internal carotid and vertebral arteries. **Physiol Meas** 26:477–488, 2005.
11. Gijsen FJ, van de Vosse FN, Janssen JD: The influence of the non-Newtonian properties of blood on the flow in large arteries: Steady flow in a carotid bifurcation model. **J Biomech** 32:601–608, 1999.
12. Hoit DA, Malek AM: Three-dimensional rotational angiographic detection of in-stent stenosis in wide-necked aneurysms treated with a self-expanding intracranial stent. **Neurosurgery** 57:1228–1236, 2005.
13. Hyun S, Kleinstreuer C, Archie JP Jr: Hemodynamics analyses of arterial expansions with implications to thrombosis and restenosis. **Med Eng Phys** 22:13–27, 2000.
14. Kasner SE, Chimowitz MI, Lynn MJ, Howlett-Smith H, Stern BJ, Hertzberg VS, Frankel MR, Levine SR, Chaturvedi S, Benesch CG, Sila CA, Jovin TG, Romano JG, Cloft HJ; Warfarin Aspirin Symptomatic Intracranial Disease Trial Investigators: Predictors of ischemic stroke in the territory of a symptomatic intracranial arterial stenosis. **Circulation** 113:555–563, 2006.
15. Kasner SE, Lynn MJ, Chimowitz MI, Frankel MR, Howlett-Smith H, Hertzberg VS, Chaturvedi S, Levine SR, Stern BJ, Benesch CG, Jovin TG, Sila CA, Romano JG; Warfarin Aspirin Symptomatic Intracranial Disease (WASID) Trial Investigators: Warfarin vs aspirin for symptomatic intracranial stenosis: Subgroup analyses from WASID. **Neurology** 67:1275–1278, 2006.
16. Kern MJ, Tron C, Donohue TJ, Bach RG, Caracciolo EA, Aguirre FV, Labovitz AJ: Hemodynamic significance of coronary jet velocity in patients: Limitations of the Bernouilli equation in small conduits. **Am Heart J** 129:887–894, 1995.
17. Kroll MH, Hellums JD, McIntire LV, Schafer AI, Moake JL: Platelets and shear stress. **Blood** 88:1525–1541, 1996.
18. Leung JH, Wright AR, Cheshire N, Crane J, Thom SA, Hughes AD, Xu Y: Fluid structure interaction of patient specific abdominal aortic aneurysms: A comparison with solid stress models. **Biomed Eng Online** 5:33, 2006.
19. Li ZY, Howarth SP, Tang T, Gillard JH: How critical is fibrous cap thickness to carotid plaque stability? A flow-plaque interaction model. **Stroke** 37:1195–1199, 2006.
20. Liu Y, Lai Y, Nagaraj A, Kane B, Hamilton A, Greene R, McPherson DD, Chandran KB: Pulsatile flow simulation in arterial vascular segments with intravascular ultrasound images. **Med Eng Phys** 23:583–595, 2001.
21. Maxwell MJ, Dopheide SM, Turner SJ, Jackson SP: Shear induces a unique series of morphological changes in translocating platelets: Effects of morphology on translocation dynamics. **Arterioscler Thromb Vasc Biol** 26:663–669, 2006.
22. Maxwell MJ, Westein E, Nesbitt WS, Giuliano S, Dopheide SM, Jackson SP: Identification of a 2-stage platelet aggregation process mediating shear-dependent thrombus formation. **Blood** 109:566–576, 2007.
23. Moffatt HK, Tsinober A: Helicity in Laminar and Turbulent Flow. **Annual Review of Fluid Mechanics** 24:281–312, 1992.
24. Neff KW, Horn P, Dinter D, Vajkoczy P, Schmiedek P, Düber C: Extracranial-intracranial arterial bypass surgery improves total brain blood supply in selected symptomatic patients with unilateral internal carotid artery occlusion and insufficient collateralization. **Neuroradiology** 46:730–737, 2004.
25. Nussbaum ES, Erickson DL: Extracranial-intracranial bypass for ischemic cerebrovascular disease refractory to maximal medical therapy. **Neurosurgery** 46:37–43, 2000.
26. Ovbiagele B, Saver JL, Lynn MJ, Chimowitz M; WASID Study Group: Impact of metabolic syndrome on prognosis of symptomatic intracranial atherostenosis. **Neurology** 66:1344–1349, 2006.
27. Perktold K, Resch M, Florian H: Pulsatile non-Newtonian flow characteristics in a three-dimensional human carotid bifurcation model. **J Biomech Eng** 113:464–475, 1991.
28. Ruggeri ZM: Platelets in atherothrombosis. **Nat Med** 8:1227–1234, 2002.
29. Ruggeri ZM, Dent JA, Saldívar E: Contribution of distinct adhesive interactions to platelet aggregation in flowing blood. **Blood** 94:172–178, 1999.
30. Ruggeri ZM, Orje JN, Habermann R, Federici AB, Reininger AJ: Activation-independent platelet adhesion and aggregation under elevated shear stress. **Blood** 108:1903–1910, 2006.
31. Samuels OB, Joseph GJ, Lynn MJ, Smith HA, Chimowitz MI: A standardized method for measuring intracranial arterial stenosis. **AJNR Am J Neuroradiol** 21:643–646, 2000.
32. Savage B, Almus-Jacobs F, Ruggeri ZM: Specific synergy of multiple substrate-receptor interactions in platelet thrombus formation under flow. **Cell** 94:657–666, 1998.
33. Savage B, Saldivar E, Ruggeri ZM: Initiation of platelet adhesion by arrest onto fibrinogen or translocation on von Willebrand factor. **Cell** 84:289–297, 1996.
34. Schafer AI, Zavoico GB, Loscalzo J, Maas AK: Synergistic inhibition of platelet activation by plasmin and prostaglandin I2. **Blood** 69:1504–1507, 1987.
35. Scheel P, Ruge C, Schöning M: Flow velocity and flow volume measurements in the extracranial carotid and vertebral arteries in healthy adults: Reference data and the effects of age. **Ultrasound Med Biol** 26:1261–1266, 2000.
36. Schirmer CM, Malek AM: Wall shear stress gradient analysis within an idealized stenosis using non-Newtonian flow. **Neurosurgery** 61:853–864, 2007.
37. Steinman DA: Image-based computational fluid dynamics: A new paradigm for monitoring hemodynamics and atherosclerosis. **Curr Drug Targets Cardiovasc Haematol Disord** 4:183–197, 2004.
38. Steinman DA, Poepping TL, Tambasco M, Rankin RN, Holdsworth DW: Flow patterns at the stenosed carotid bifurcation: Effect of concentric versus eccentric stenosis. **Ann Biomed Eng** 28:415–423, 2000.
39. Tang D, Yang C, Kobayashi S, Ku DN: Steady flow and wall compression in stenotic arteries: A three-dimensional thick-wall model with fluid-wall interactions. **J Biomech Eng** 123:548–557, 2001.
40. Thurston GB: Rheological parameters for the viscosity viscoelasticity and thixotropy of blood. **Biorheology** 16:149–162, 1979.
41. Womersley JR: Method for the calculation of velocity, rate of flow and viscous drag in arteries when the pressure gradient is known. **J Physiol** 127:553–563, 1955.
42. Young DF, Cholvin NR, Roth AC: Pressure drop across artificially induced stenoses in the femoral arteries of dogs. **Circ Res** 36:735–743, 1975.

Acknowledgments

This work was supported by the Boston Institute of Neurosurgery and by a grant from the Cam Neely Foundation.

COMMENTS

This study shows how advanced computational fluid dynamics and modeling of blood vessels have become. The videos are stunningly beautiful. At one time, these systems could not account for pulsatile flow and non-Newtonian fluids. Schirmer and Malek use state-of-the-art methods to model blood flow through intracranial stenoses. They account for the exact geometry of the stenoses, pulsatile flow, and the non-Newtonian nature of blood flow. One feature still not incorporated is the change in diameter of the arteries with blood flow. Arteries are not rigid tubes although, in the setting of atherosclerosis in the patients modeled here, that may not be a major problem as the arteries may be very rigid.

The main question here is what we will learn from this kind of modeling. The present analysis seems to show that modeling can produce results that reflect clinical phenomena as opposed to giving any new biological mechanistic insights. That being said, an example of a modeling technique that concluded that one needed to postulate another biological process was the modeling of vascular beds (1). The modeling techniques are also improving and, as computing power and mathematics advance, modeling may soon reflect reality, which is exciting and will certainly lead to important advances in the study of cerebral vasculature.

R. Loch Macdonald
Toronto, Canada

---

1. Pries AR, Reglin B, Secomb TW: Structural adaptation of microvascular networks: Functional roles of adaptive responses. **Am J Physiol Heart Circ Physiol** 281:H1015–H1025, 2001.

The authors have shown that flow patterns in complex intracranial atherosclerotic lesions are predicted to cause wall shear stress in a range sufficient to cause platelet activation and distal embolization. If carried forward, this work may enable us to better predict which asymptomatic lesions may be at greatest risk for future problems, yielding a valuable risk stratification tool. In addition, these models may enable one to predict the effect of treatment via endovascular stenting, further aiding in selecting patients for treatment. Of course, there are limitations with any model, and plaque heterogeneity is an important issue in this model. More work to validate this model in vivo would be quite useful. Pre- and postprocedural assessments of flow patterns using tools such as quantitative magnetic resonance angiography would be a useful step towards this end.

Bob Carter
Boston, Massachusetts

This is an elegant study of fluid dynamics in a model based on an actual three-dimensional rendition of intracranial stenotic lesions from patients undergoing rotational angiography before and after stenting. The fluid dynamic methods are rigorous, including the non-Newtonian fluid modeling and the use of the contralateral artery as a control. We are introduced to new terms, such as "vorticity" and "helicity," which are typically more familiar to fluid engineers.

The findings confirm what has already been reported in extracranial plaques and other vascular beds, whereby significant pressure gradient, turbulence, and shear stress arise as stenosis severity exceeds 75% range. Yet it is not clear if these changes are truly worse or different in intracranial stenoses than with extracranial carotid plaques of similar severity; it would have been nice to have examined extracranial stenoses as another control. Also, although the range of shear stresses has been associated with platelet activation, their actual "deleterious effects" and "clinical consequences" remain speculative and mere hypotheses to be tested in future studies. Therapeutic implications, especially with regard to the potential risk/benefit ratio of stenting versus antiplatelet therapies cannot be sold without further testing, despite the sexy packaging of engineering terminology.

Issam A. Awad
Evanston, Illinois

In this article, the authors study high-resolution digital rotational angiography of nine atherosclerotic lesions, including six carotid arteries, two vertebral arteries, and one middle cerebral artery, and perform reconstructions based on this data set for a computation computerized analysis of flow. The major study results suggest that the complex flow patterns within real atherosclerotic lesions include shear rates greater than 19,000, which is felt to be high enough to single-handedly induce high shear platelet activation. The results were marked changes in pressure gradients and flow decelerations with these larger degrees of stenosis, which were not seen in nondistorted regions. The authors feel that some of these flow characteristics are improved with stenting and improvement of diameter of the channel. This study is extremely interesting. It needs to emphasize several points to improve. The physiology of the vessels is more complex than a stiff model as used here, but is rather dynamic. This line of investigation studies the flow channel rather than the lesion itself, which tells us relatively little about many embolic sources from unstable plaques. The authors must explain the relative contribution of shear in light of other causes of symptoms. The shear forces, however, may be important for our understanding of endothelial damage, fissuring, and embolization of portions of the plaque. The flow dynamic principles may also help explain plaque formation, not just platelet adherence, as shear above 10,000 is easily achieved in the higher-grade lesions. Finally, they should especially not mistake this particular evidence as being generalized throughout all patient populations. It is believed that this application of physics and engineering to the understanding of flow is most important and hopefully more results will be forthcoming.

Robert J. Dempsey
Madison, Wisconsin

SUBMISSIONS, PEER-REVIEW, AND DISCLOSURE

All original material presented in NEUROSURGERY, Operative NEUROSURGERY, and NEUROSURGERY-*Online* undergoes rigorous multi-factorial peer-review by carefully selected panels of knowledgeable and dedicated individuals who are highly versed in the academic process and the given topic.

For some time the burden of full disclosure of financial or other personal interests that may bias presentation has been placed on submitting authors. NEUROSURGERY will now extend this strict requirement of disclosure to those engaged in the review process in an effort to reduce bias and potential conflict in analysis and decision-making.